

Warm Ice Giant GJ 3470b. II Revised Planetary and Stellar Parameters from Optical to Near-infrared Transit Photometry

Lauren I. Biddle¹, Kyle A. Pearson¹, Ian J. M. Crossfield², Benjamin J. Fulton⁴, Simona Ciceri², Jason Eastman⁵, Travis Barman⁷, Andrew W. Mann⁴, Gregory W. Henry⁶, Andrew W. Howard⁴, Michael H. Williamson⁶, Evan Sinukoff⁴, Diana Dragomir⁵, Laura Vican⁸, Luigi Mancini², John Southworth¹¹, Adam Greenberg⁸, Jake D. Turner⁹, Robert Thompson¹, Brian W. Taylor¹², Stephen E. Levine^{3,10}, Matthew W. Webber¹⁰

ABSTRACT

It is important to explore the diversity of characteristics of low-mass, low-density planets to understand the nature and evolution of this class of planets. We present a homogeneous analysis of 12 new and 9 previously published broadband photometric observations of the Uranus-sized extrasolar planet GJ 3470b, which belongs to the growing sample of sub-Jovian bodies orbiting M dwarfs. The consistency of our analysis explains some of the discrepancies between previously published results and provides updated constraints on the planetary parameters. Our data are also consistent with previous transit observations of this system. The physical properties of the transiting system can only be constrained as well as the host star is characterized, so we provide

¹University of Arizona Department of Astronomy, 933 N. Cherry Street, Tucson, AZ, 85721, USA, lbiddle@email.arizona.edu

²Max-Planck Institut für Astronomie, Königstuhl 17, D-69117, Heidelberg, Germany

³Lowell Observatory, 1400 West Mars Hill Road, Flagstaff, AZ 86001, USA

⁴Institute for Astronomy, University of Hawaii at Manoa, 2680 Woodlawn Drive, Honolulu, HI 96822, USA

⁵Las Cumbres Observatory Global Telescope Network, 6740 Cortona Drive, Suite 102, Santa Barbara, CA 93117, USA

⁶Center of Excellence in Information Systems, Tennessee State University, 3500 John A. Merritt Blvd., Box 9501, Nashville, TN 37209, USA

⁷Department of Planetary Sciences, Lunar and Planetary Laboratory, University of Arizona, Tucson, AZ, 85721, USA

⁸Division of Astronomy and Astrophysics, University of California Los Angeles, 430 Portola Plaza, Los Angeles, CA 90095, USA

⁹Department of Astronomy, University of Virginia, 1721 University Avenue, Charlottesville, VA, 22903, USA

¹⁰Department of Earth, Atmospheric and Planetary Sciences, Massachusetts Institute of Technology, 77 Massachusetts Avenue, Cambridge, MA 02139, USA

¹¹Astrophysics Group, Keele University, Staffordshire, ST5 5BG, UK

¹²Boston University, Astronomy Department, 725 Commonwealth Ave., Boston, MA 02215

new spectroscopic measurements of GJ 3470 from 0.33 to 2.42 μm to aid our analysis. We find $R_\star = 0.48 \pm 0.04 R_\odot$, $M_\star = 0.51 \pm 0.06 M_\odot$, and $T_{\text{eff}} = 3652 \pm 50$ K for GJ 3470, along with a rotation period of 20.70 ± 0.15 d and an R-band amplitude of 0.01 mag, which is small enough that current transit measurements should not be strongly affected by stellar variability. However, to report definitively whether stellar activity has a significant effect on the light curves, this requires future multi-wavelength, multi-epoch studies of GJ 3470. We also present the most precise orbital ephemeris for this system: $T_o = 2455983.70472 \pm 0.00021$ BJD_{TDB}, $P = 3.3366487_{-0.0000033}^{+0.0000043}$ d, and we see no evidence for transit timing variations greater than 1 minute. Our reported planet to star radius ratio is 0.07642 ± 0.00037 . The physical parameters of this planet are $R_p = 3.88 \pm 0.32 R_\oplus$, and $M_p = 13.73 \pm 1.61 M_\oplus$. Because of our revised stellar parameters, the planetary radius we present is smaller than previously reported values. We also perform a second analysis of the transmission spectrum of the entire ensemble of transit observations to date, supporting the existence of a H₂ dominated atmosphere exhibiting a strong Rayleigh scattering slope.

Subject headings: infrared: stars — planetary systems — stars: individual (GJ 3470)
— techniques: photometric — techniques: spectroscopic — eclipses

1. Introduction

It is important to pursue detailed characterization of extrasolar planets between Earth and Neptune-mass because these bodies have no solar system analogue, and may provide key insight to the mechanisms of formation and evolution of planetary systems. The Kepler mission has discovered over 2,300 planet candidates as of February 2012 (Batalha et al. 2013), analysis of which yields increasing occurrence with decreasing planet radius (Dressing & Charbonneau 2013; Howard et al. 2012; Dong & Zhu 2012). Despite the relative abundance of sub-Jovian exoplanets, few have been characterized in great detail. The majority of the Kepler candidates pose a challenge when detecting transits from the ground because they do not meet the criteria for sufficient precision capabilities (e.g., they lack either a large planet-to-star radius ratio or a bright host star). However, these requirements are fulfilled for planets that transit nearby M dwarfs. These systems allow significantly smaller extrasolar planets to be studied with greater precision because they exhibit larger transit depths (Gillon et al. 2007; Deming et al. 2007; Demory et al. 2007) than if they were to orbit a larger, dimmer star. *Per contra*, such observationally favorable systems that exhibit a deep transit are relatively rare. So far, the only other small, low-mass planets that can be thoroughly characterized are GJ 436b (Gillon et al. 2007; Butler et al. 2004), GJ 1214b (Charbonneau et al. 2009), and HD 97658b (Dragomir et al. 2013; Howard et al. 2011) with the exception of 55 Cnc e, which orbits a solar type star (McArthur et al. 2004; Dawson & Fabrycky 2010; Winn et al. 2011; Demory et al. 2011). It is essential to probe this population to compare these systems’ properties with those of the more thoroughly studied hot Jupiters so that we may develop our understanding

of formation mechanisms of planets linking Earth and Jupiter analogues.

A recent addition to this collection of exoplanets is GJ 3470b (Bonfils et al. 2012), a warm ice giant roughly the size and mass of Uranus orbiting a nearby M dwarf. This system exhibits a sufficiently large transit depth to make detailed characterization of the planet feasible. Previous studies of GJ 3470b probe the planet’s atmospheric composition: Fukui et al. (2013) present optical transit photometry and tentatively claim the planet does not have a thick cloud layer. Crossfield et al. (2013) presented K-band transit spectroscopy and found a flat transmission spectrum consistent with a hazy, methane-poor, or high metallicity atmosphere. Optical photometry indicates a strong Rayleigh-scattering slope at short wavelengths also consistent with a hazy atmosphere (Nascimbeni et al. 2013).

Several effects can interfere with measurements, posing limitations on our understanding of GJ 3470b’s bulk properties and atmospheric constraints. For example, when occulted by the planet, star spots introduce wavelength-dependent perturbations into the light curve and the resulting transit parameters (e.g., Pont et al. 2007; Rabus et al. 2009). Unocculted star spots can have an effect on the transit depth, making it appear larger than it would without stellar activity (Guillot & Havel 2011; Jordán et al. 2013). Furthermore, the amount of star spots visible on the Earth-directed face of the star varies over time because of stellar rotation and star spot evolution, and will be different for observations taken over several epochs (e.g., Czesla et al. 2009; Knutson et al. 2011; Pont et al. 2013). To account for these factors, we utilize long-term photometric monitoring to assist in identifying these time-dependent changes in stellar brightness, and our results predict a weak systematic effect on the data due to stellar activity.

Our photometric campaign of GJ 3470b, consisting of 12 new transit observations in conjunction with 9 previously published light curves, aims to enhance measurements of planetary radius and mass, in addition to placing further constraints on the planetary atmosphere. The analysis also provides an improved ephemeris, which can assist in the eventual search for additional planetary bodies in the GJ 3470 system via observed variations in transit timing (Holman & Murray 2005; Agol et al. 2005). A repercussion of photometric follow-up of planetary systems is the opportunity to provide more accurate estimates of stellar properties. Improved constraints on GJ 3470 increases the precision with which we can derive planetary parameters. Thus, we also present revised stellar parameters that improve upon those previously derived for GJ 3470 (Bonfils et al. 2012; Demory et al. 2012; Fukui et al. 2013; Pineda et al. 2013) using visible and near-IR spectra.

In this paper we provide improved planetary, orbital and stellar parameters for the GJ 3470 system. We also include a revision of stellar properties, and possible sources of systematic error. We begin with host star characterization in Section 2, which includes data acquisition, reduction processes and results. In Section 3 we describe observations, data calibration, and results for the planetary system. Discussion of the significance of these results takes place within Section 4. We conclude in Section 5.

2. Stellar Spectroscopy and Long-Term Photometric Monitoring

Having detailed knowledge of an exoplanet’s host star is crucial in the understanding of the planetary system. Properties such as planet mass and radius are determined only as precisely as the corresponding stellar properties are known. Bulk and spectral properties help constrain the system age and stellar metallicity, and potentially help determine conditions that influence the formation of planetary systems. The following section describes our observations of GJ 3470, which we use to characterize the stellar parameters in [Section 4.1](#).

The stellar spectra obtained with IRTF/SpeX ([Section 2.1.1](#)) and UH/SNIFS ([Section 2.1.2](#)) are plotted in a single figure ([Figure 1](#)). These data are also available as an electronic supplement.

2.1. Spectroscopic Observations and Data Reduction

2.1.1. IRTF (3 m)/SpeX

We observed GJ 3470 with SpeX ([Rayner et al. 1998](#)) at the 3 m NASA IRTF on UT 2013-02-28, and obtained spectra from $0.9 - 2.4\mu\text{m}$ using a $0.3''$ slit, which provides spectral resolution of roughly 2,000. We obtained 20 frames, each of 20 s duration. Observations were obtained with the slit aligned at the parallactic angle. Data reduction followed previously-described methods ([Rayner et al. 2009](#); [Crossfield 2012](#)); in brief, we used the XSpeXTool package ([Cushing et al. 2004](#)) to calibrate raw frames, extract spectra from nod-subtracted frames, correct for telluric absorption using observations of the A0V star HD 58296 (obtained at slightly higher airmass: 1.17 vs. 1.13), and combine multiple echelle orders into a single spectrum. The final signal-to-noise (SNR) of our spectrum ranges from 150–370 pix^{-1} . We flux-calibrate the spectrum using previously-described methods ([Rayner et al. 2009](#)).

2.1.2. UH (2.2 m)/SNIFS:

Optical spectra of GJ 3470 were obtained from $0.33 - 0.9\mu\text{m}$ with the SuperNova Integral Field Spectrograph (SNIFS, [Aldering et al. 2002](#); [Lantz et al. 2004](#)) on the University of Hawaii 2.2m telescope atop Mauna Kea. SNIFS separates the incoming light into blue (3200 \AA to 5200 \AA) and red (5100 \AA to 9700 \AA) spectrograph channels, yielding resolutions of $\simeq 800$ and $\simeq 1000$, respectively. An integration time of 85 s was sufficient to achieve a peak SNR of $\simeq 200 \text{ pix}^{-1}$ in the red and $\simeq 70$ in the blue.

The SNIFS pipeline ([Bacon et al. 2001](#); [Aldering et al. 2006](#)) performed basic reduction, including bias, flat-field, and dark corrections. The spectrum was wavelength calibrated using arc lamp exposures taken at the same telescope pointing and time as the science data. Over the course of each night, we obtained spectra of the EG131 and Feige 110 spectrophotometric standards ([Bessell](#)

1999; Hamuy et al. 1992; Oke 1990). We combined a model of telluric absorption from Buton et al. (2013) with standard star observations to correct each spectrum for instrument response and atmospheric extinction. We shifted each spectrum in wavelength to the rest frames of their source stars by cross-correlating each spectrum to a spectral template of similar spectral type from the Sloan Digital Sky Survey (Stoughton et al. 2002; Bochanski et al. 2007). More details on our data reduction can be found in Mann et al. (2012) and Lépine et al. (2013).

2.2. Long-Term Photometric Monitoring

We obtained nightly photometry of GJ 3470 with the Tennessee State University Celestron C14 0.36 m Automated Imaging Telescope (AIT) located at Fairborn Observatory in southern Arizona (Henry 1999; Eaton et al. 2003). The AIT is equipped with an SBIG STL-1001E CCD camera and a Cousins R filter. Each observation consists of 4–10 consecutive exposures on a field containing GJ 3470 and several surrounding comparison stars. The individual frames are then co-added and reduced to differential magnitudes (i.e., GJ 3470 minus the mean brightness of the comparison stars). Each nightly observation is also corrected for differential extinction. A total of 246 nightly observations (excluding transit observations) were collected between 2012 December 10 and 2013 May 27.

The nightly out-of-transit observations range over 169 days of the 2012–2013 observing season and are plotted in the top panel of Figure 2. Brightness variability with a period of ~ 20 days and an amplitude of ~ 0.01 mag is easily seen by inspection of the light curve. A frequency spectrum, based on the least-squares fitting of sine curves to unequally spaced observations, was computed via the method of Vaníček (1971) and plotted in the middle panel of Figure 2 as the reduction of the variance in the data vs. trial period. The best frequency corresponds to a period of 20.70 ± 0.15 days, where the uncertainty is estimated from the width of the highest peak. We take this to be the star’s rotation period, made apparent by rotational modulation in the visibility of star spots. This rotation period agrees well with the low $v \sin(i)$ measured by Bonfils et al. (2012). The observations are replotted in the bottom panel phased with the rotation period and overlaid with a least-squares sine fit to the phased observations. The peak-to-peak amplitude is only 0.010 mag suggesting that analysis of the transit observations will not have to deal with complications caused by the planetary occultation of large spots. The sine-curve fit in the bottom panel is converted to HJD and overlaid on the observations in the top panel, and shows good coherence in spite of the small spot amplitude. Henry et al. (1995) show additional detections of low-level brightness variability in several dozen moderately active stars.

We phased the photometric observations to the radial velocity period and computed a new least-squares sine fit to the radial velocity period. The formal peak-to-peak amplitude is 0.00059 ± 0.00099 mag. This is consistent with the lack of detection of the photometric signal in the radial velocities of Bonfils et al. (2012) and confirms that radial velocity variations in GJ 3470 are indeed due to planetary reflex motion and not line-profile variations due to spots (e.g., Queloz et al. 2001;

Paulson et al. 2004). Furthermore, these variations support there is no consequential systematic effect on the transit light curves (see Section 4.1.3).

3. Transit Light Curves: Data & Analysis

In this section we describe our observations and calibration methods. We also discuss our light curve analysis procedure and results.

3.1. Photometric Observations and Analysis

We obtained 12 total light curves (5 full and 7 partial), in which many of the events were observed with multiple facilities. We also include 9 light curves previously analyzed by Bonfils et al. (2012), Fukui et al. (2013), and Nascimbeni et al. (2013) for a total of 21 light curves analyzed homogeneously. All light curves analyzed in this work are plotted in Figure 3, and the corresponding residuals are displayed in Figure 4. Observational details including integration time, airmass range, and median seeing are summarized in Table 1, and the data acquisition process and reduction methods are described below.

3.1.1. Discovery Channel Telescope (4 m)

We observed a full transit during early science observations with the Discovery Channel Telescope’s Large Monolithic Imager (LMI), an E2V CCD-231, 6k×6k, deep depletion CCD and a field of view (FOV) of 12.3’×12.3’. Data were taken with the LMI’s Cousin I filter¹. Ingress occurred as GJ 3470 was rising (airmass 1.8) so the pre-ingress photometry exhibitshigher scatter than the subsequent data. Because DCT’s audible warning alarms had not yet been activated, a partial dome occultation occurred in the middle of the transit and we excise these data from the subsequent analysis. Observations were made with a significant amount of defocus in order to maximize integration times and reduce overheads. To avoid possible systematic drifts from the LMI’s four-quadrant readout we measure photometry only for GJ 3470 and 2 comparison stars lying within a single quadrant of the detector. We investigate a wide range of aperture sizes, and in the final analysis use a 10” photometric aperture that minimizes the scatter in the resulting light curve. This observation is denoted as transit number 11 as seen in Table 1.

¹See <http://www.lowell.edu/techSpecs/LMI/I.eps>

3.1.2. *Kuiper (1.55 m)*

Three transit observations were conducted at the Steward Observatory Kuiper Telescope in Arizona using the Mont4k CCD 4096×4096 pixel sensor with a FOV of 9.7′×9.7′ using the red, Arizona-I optical filter. Two transits were obtained under poor weather conditions, which was the source of significant amount of scatter in both light curves, yielding extremely low quality data, so we present the one good light curve (number 15), which was acquired on a clear night.

To reduce the data we used the Exoplanet Data Reduction Pipeline, ExoDRPL, described by [Pearson et al. \(2013\)](#). We performed standard IRAF aperture photometry using eight comparison stars at 110 different aperture radii. After all combinations of comparison stars were tested, we found that a 6.02″ aperture radius and one comparison star of much the same brightness as GJ 3470 provided the lowest scatter in the pre- and post-transit baseline. We produce a synthetic light curve by averaging the light curves from our reference stars, and normalize the final light curve of GJ 3470b by dividing by this synthetic light curve.

3.1.3. *LCOGT (1 m and 2 m)*

We observed three full and three partial transits using telescopes of the Las Cumbres Observatory Global Telescope (LCOGT) network. All LCOGT 1.0 m data were obtained using an SBIG STX-16803 4096×4096 CCD with 0.464″ square pixels (2×2 binning), a 15.8′×15.8′ field of view, and processed using the pipeline described in [Brown et al. \(2013\)](#). Two full transits taken in r′ and PanStarrs-Z bands were acquired with two of the 1.0 m telescopes at the LSC node of the network at the Cerro Tololo Inter-American Observatory (CTIO) in Chile. Two partial transits were observed in Sloan r′, and a full transit was acquired in the i′ band using the 1.0 m telescope at the ELP node of the network at McDonald Observatory in Texas. The i′ band observations were defocused slightly.

We obtained a partial transit with the 2.0-m Faulkes Telescope North (FTN), a part of the LCOGT’s network of robotic telescopes, using a Fairchild CCD486 BI 4k x 4k Spectral Imaging camera with a FOV of 10.5′ x 10.5′ ([Brown et al. 2013](#)) in the Bessel-B filter. We defocused the telescope moderately in order to avoid saturation and we increased the open shutter time relative to the overhead time. The light curves were extracted through aperture photometry using 5.5″ aperture radii, eight comparison stars for the r′ band observation number 18, and seven comparison stars for i′ and r′, 20 and 21. We also perform differential photometry using the weighted average of two, six, and seven comparison stars for the r′, Panstarrs-Z, and B time series (9, 10, and 17), respectively. The weather during all observation nights was clear with the exception of transit 18.

3.1.4. Lick/Nickel (1 m)

We observed a total of six observations at the Nickel Telescope at Lick Observatory using the CCD-2 Direct Imaging Camera with a 2048×2048 pixel CCD and a FOV of $6.3' \times 6.3'$, with the Gunn Z filter. We omit three of these observations because they were taken under poor weather conditions and resulted in low quality light curves. We do present one full light curve (transit 08) and two partial light curves (transits 12 and 16). All observations were defocused, and counts were kept below 35,000 to preserve linearity. We performed standard aperture photometry methods using two comparison stars of similar magnitude to GJ 3470, and a set of custom IDL routines that were also used for the previous analysis of transit light curves obtained at this facility (Johnson et al. 2011). We selected aperture radii for each light curve that minimized scatter.

3.1.5. Calar Alto/Zeiss (1.23 m)

We observed a partial transit using the Zeiss telescope at the German-Spanish Calar Alto Observatory with the Cousins I filter using a DLRMKIII camera, equipped with an E2V CCD231-84-NIMO-BI-DD sensor, $4k \times 4k$ pixels and a FOV of $21' \times 21'$, which was already successfully employed to investigate several transiting planets (Mancini et al. 2013; Ciceri et al. 2013). We observed the ingress phase of the transit, but the emergence of clouds prevented us from observing the remainder of the event.

We analyzed the data using a version of the DAOPHOT reduction pipeline (Stetson 1987; Southworth et al. 2009). Aperture photometry is then performed using the IDL task, Aper, which is part of NASA’s ASTROLIB subroutine library, and we account for pointing variations by cross-correlating each image against a reference image. We chose the aperture size and four comparison stars that yielded the lowest scatter in the final differential photometry light curve. The relative weights of the comparison stars were optimized simultaneously by fitting a second-order polynomial to the outside-transit observations to normalize them to unit flux.

3.2. Methods

To fit our light curves we use the Transit Analysis Package (TAP), an IDL fitting software written by Gazak et al. (2012). TAP uses Markov Chain Monte Carlo (MCMC) techniques to fit light curves by utilizing the analytical model of Mandel & Agol (2002). While performing the analysis, we ran 100,000 MCMC steps. TAP assesses the uncertainties using the wavelet based likelihood function developed by Carter & Winn (2009), where “red” noise is the time-correlated Gaussian scatter, and “white” noise is the uncorrelated Gaussian scatter.

For the analysis process, we allowed the scaled semi-major axis, a/R_* , period, P, and inclination, i , to vary freely, but required they be consistent for the entire dataset. The mid-transit time,

T_o , could float for each transit, under the requirement that all events are related to each other by a linear ephemeris. We linked the planet to star radius ratio, R_p/R_\star , for all transits taken with comparable bandpasses to measure transit depths as a function of wavelength. We accounted for limb darkening by using quadratic law limb darkening coefficients and corresponding uncertainties calculated using the Monte Carlo approach described by [Crossfield et al. \(2013\)](#), who derive these values using $T_{\text{eff}} = 3500$ K, surface gravity of 10^5 cm s^{-2} , and solar abundances. The limb darkening coefficients varied with Gaussian priors using the coefficients and uncertainties described above, and listed in [Table 2](#). [Bonfils et al. \(2012\)](#) report a 1-sigma upper limit on GJ 3470b’s orbital eccentricity, e , of 0.051. Using the Systemic tool ([Meschiari et al. 2009](#)), we estimated that the posterior distribution of orbital eccentricity from the RV discovery data is approximately described by a normal distribution (truncated below zero) with mean 0.009 and dispersion 0.088, consistent with a circular orbit. We used these values to impose a Gaussian prior on e for the light curve analysis in TAP.

3.3. Results

The results of the analysis, including R_p/R_\star and T_o for each light curve, are listed in [Table 1](#). The updated system parameter, a/R_\star equals $13.94^{+0.44}_{-0.49}$. We found $P = 3.3366487^{+0.0000043}_{-0.0000033}$ d, and $i = 88.88^{+0.62}_{-0.45}$ deg. Under the assumption there is no wavelength dependence, we take the weighted mean of our wavelength-dependent transit depth measurements, and we find R_p/R_\star equals 0.07642 ± 0.00037 . These values are tabulated in [Table 3](#). The uncertainty on our measurement of R_p/R_\star is larger than that expected to result from stellar variability (see [Section 4.1.3](#)), so GJ 3470’s intrinsic variability is unlikely to significantly affect these results.

Using our mid-transit times along with the mid-transit times from [Demory et al. \(2013\)](#), [Crossfield et al. \(2013\)](#), we fit a new linear transit ephemeris, ($T_o = 2455983.70472 \pm 0.00021$ BJD_{TDB}, $P = 3.3366487^{+0.0000043}_{-0.0000033}$ d). We plot the epoch of each transit against the observed time minus the calculated time (O-C) in [Figure 5](#). If there were another body orbiting GJ 3470, we might observe a transit timing variation due to its gravitational effects on GJ 3470b. Any detectable TTVs must lie outside the timing range labeled in green in [Figure 5](#), which signifies the upper and lower limits of non-transit variations within 1σ of the error of the period. Any values lying outside of this region indicate deviations from the linear ephemeris as a result of another body in the system. The data point corresponding to Transit 1 does lie outside the region described above, however this transit coincides with a low quality, partial light curve, so we disregard this point as a TTV. We find no apparent TTVs in the available data, and within the precision of our measurements.

4. Discussion

The following section discusses implications of the results of stellar characterization, physical system parameters and atmospheric characterization using optical to near-IR transit spectroscopy.

4.1. Stellar Characterization

4.1.1. Physical Parameters

We determine the metallicity of GJ 3470 using the prescription from [Mann et al. \(2013a\)](#), who provide empirical relations between M dwarf metallicity, $[\text{Fe}/\text{H}]$, and the strength of molecular and atomic features in visible, J –, H –, and K –bands. We adopt the error-weighted mean of metallicities from each of these relations, accounting for both random and systematic errors. This yields a $[\text{Fe}/\text{H}]$ of $+0.18 \pm 0.08$.

We deduce the effective temperature, radius, and mass of GJ 3470 by following the procedures in [Mann et al. \(2013b\)](#). To summarize, we compared the optical spectrum to the BT-SETTL version of the PHOENIX atmospheric models ([Allard et al. 2013](#)) after masking out a few poorly modeled regions (e.g., TiO at 6500\AA). This technique has been shown to reproduce temperatures derived from the bolometric flux and angular diameter of nearby stars ([Boyajian et al. 2012](#)) to $\simeq 60$ K, which we adopt as the error on our effective temperature. We utilize additional empirical relations from [Mann et al. \(2013a\)](#) relating stellar effective temperature, mass, and radius from nearby stars to calculate the other physical characteristics of the star. We find the stellar effective temperature, $T_{\text{eff}} = 3682 \pm 60$ K, stellar radius, $R_{\star} = 0.48 \pm 0.04 R_{\odot}$, and stellar mass, $M_{\star} = 0.51 \pm 0.06 M_{\odot}$.

Under the assumption the planet’s orbit is circular, we employed the formula by [Seager & Mallén-Ornelas \(2003\)](#) to independently estimate the stellar density, ρ_{\star} , which follows directly from inverting Kepler’s 3rd law of motion by substituting in the expression for mean density in place of mass:

$$\rho_{\star} = \frac{3\pi}{GP^2} \left(\frac{a}{R_{\star}} \right)^3 - \rho_p \left(\frac{R_p}{R_{\star}} \right)^3, \quad (1)$$

where G is the gravitational constant, P is the orbital period and the second term on the right is typically negligible. We find $\rho_{\star} = 3.27^{+0.31}_{-0.34} \rho_{\odot}$. These values are tabulated in [Table 4](#).

Our results for the radius of GJ 3470 obtained using the stellar spectrum are lower by more than 1σ than the radii found by [Fukui et al. \(2013\)](#) ($0.526 \pm 0.023 R_{\odot}$) and [Demory et al. \(2012\)](#) ($0.568 \pm 0.037 R_{\odot}$). Our values given above for R_{\star} and M_{\star} alone return a mean bulk density of $4.62 \pm 1.10 \rho_{\odot}$, roughly 3σ greater than the value derived from our light curve analysis. We bring attention to the discrepancy in our stellar density derived using the photometric data versus the stellar spectrum. This density offset could indicate a systematic bias caused by occulted or unocculted star spots, which can be tested by repeated observations and by observations at longer wavelengths. The discrepancy could also be caused by an eccentric orbit, which can be tested

further with RV measurements or by determining the time of GJ 3470b’s secondary eclipse. Our results support that light curves of transiting planets can help place constraints on the properties of their host stars. However, stellar activity is likely not a contributing factor in our observations because, as mentioned in [Section 4.1.3](#), it is unlikely to pose a significant systematic effect for transit observations, which drives home the necessity of advancing our understanding of M dwarf stars.

In [Table 3](#), we present the the final value of ρ_* , which is the weighted mean of both values in this work, deduced from the light curves and spectra. Also provided in [Table 3](#) are the resultant values for the weighted mean of all previously published stellar effective temperatures and metallicities displayed in [Table 4](#), which also lists R_* , M_* , ρ_* for all published studies.

4.1.2. Distance to GJ 3470

We calculate a distance of 28.82 ± 2.53 pc, which is consistent with, and more precise than the value calculated by [Pineda et al. \(2013\)](#) ($29.2^{+3.7}_{-3.4}$ pc). Our distance is derived from the fundamental relation between bolometric flux and luminosity ($L_{bol} = 4 \pi d^2 F_{bol}$). We use our derived stellar parameters, R_* and T_{eff} (listed in [Table 3](#)), to calculate the luminosity for GJ 3470 ($L_{bol} = 4\pi R_*^2 \sigma T_{eff}^4$). To calculate F_{bol} we integrate the spectrum presented in [Section 2](#) and [Figure 1](#) from 0.33 to 2.42 μm . For the mid-infrared we use the WISE photometric measurements of GJ 3470, converting the WISE infrared magnitudes into units of flux density using the flux zero points and effective wavelengths given in [Wright et al. \(2010\)](#). We sum the flux between the WISE data points using a linear relation between each pair of adjacent points and add it to our previous flux value. We propagated the errors associated with each photometric point using the formula obtained by taking a Taylor expansion for the trapezoidal rule.

To account for the missing flux between the two data sets, we scaled a PHOENIX BT-SETTL model ([Allard et al. 2011](#)) to our measured spectrum and added the integrated model flux between 2.42 to 3.35 μm to the pre-existing bolometric flux obtained using the two spectra. The model used was interpolated from the four nearest spectra in the BT-SETTL compilation to resemble GJ 3470 using the specified parameters $T_{eff} = 3652 \pm 50$ K, $\log_{10}(g) = 4.78 \pm 0.12$ and $[\text{Fe}/\text{H}] = 0$. To determine the resulting error associated with incorporating the model flux, we scaled the pre-existing error to the percentage of the total additional flux compared to the initial, observed flux (1.063).

Furthermore, to account for the fractional flux shortward of 0.3 μm and longward of 22 μm we scaled our bolometric flux by 1.0362 (determined by the fraction of flux in those regions compared to total stellar flux using the BT-SETTL model). We refrain from altering our uncertainty because the fraction of flux in those regions was much smaller than our other uncertainties and is negligible. We find an apparent bolometric flux of 1.42×10^{-9} [$\text{erg cm}^{-2} \text{s}^{-1}$]. The uncertainty on F_{bol} is a few percent, based on systematic uncertainties in calibrating ground-based spectra ([Rayner et al.](#)

2009).

To confirm our calculations, we determined an appropriate geometric scale factor by integrating our measured spectrum, BT-SETTL model and WISE data (where applicable) over three different contiguous bandpasses (0.6-0.8 μm , 2.1-2.3 μm and 3.3-4.6 μm) and found the mean ratio between the two quantities. The geometric scale factor is proportional to $(R_*/\text{dist})^2$ and using our previously derived value for R_* , we found that the distance is consistent with our previously derived value. Additionally, we find the values above also yield a distance consistent with that derived using optical bolometric corrections in Flower (1996).

4.1.3. *Stellar Variability, Rotation and Age*

GJ 3470’s 20 d rotation period (described in Section 2.2) permits an independent estimate of the star’s age, previously estimated to be 0.3–3 Gyr (Bonfils et al. 2012). Analysis of Kepler photometry of M dwarf rotation periods shows two distinct groups of stars, with an inferred age ratio between the groups of ~ 2.5 –3 (McQuillan et al. 2013). GJ 3470’s rotation period places it in the more rapidly-rotating group; assuming that the slower rotators have ages of 5–10 Gyr then GJ 3470 has an age of roughly 2–4 Gyr. This gyrochronological age is also broadly consistent with the MEarth survey’s analysis of M stars’ rotation periods (Irwin et al. 2011). Alternatively, we note also that GJ 3470’s rotation period is roughly 1.5 times longer than observed for stars with comparable $V - K$ colors in the 0.6 Gyr Hyades and Praesepe clusters (Delorme et al. 2011). Assuming a rotational braking index of 0.5–0.6, the relations of Meibom et al. (2009) imply an age of roughly 1.3 Gyr. We therefore estimate GJ 3470’s age to be 1–4 Gyr, consistent with but slightly older than previous estimates (Bonfils et al. 2012).

Using the formalism of Berta et al. (2011), our measurement of $\sim 1\%$ peak-to-valley variability in GJ 3470 implies a time-dependent, spot-induced variability in the R band transit depths of 5×10^{-5} over the star’s rotation period. Assuming that the spots are 300 K cooler than the stellar photosphere, this effect is roughly 20% larger in B band and roughly three times smaller at Warm Spitzer wavelengths. This amplitude is smaller than the transit precision from our ensemble of light curves. The precision of the 4.5 μm transit measurement from Spitzer (Demory et al. 2013) is also larger than our estimate. Future multi-wavelength, multi-epoch studies of GJ 3470b’s transits will determine whether stellar activity poses a significant systematic effect for transit observations of this system.

4.2. **Physical Properties of the Planetary System**

The values derived from our data analysis (see Table 3) were used to calculate the planetary parameters of GJ 3470b, including its mass, radius, density, equilibrium temperature, surface gravity and semi-major axis.

We adopted the formula by [Southworth et al. \(2007\)](#) to calculate the surface gravitational acceleration, g_p :

$$g_p = \frac{2\pi}{P} \left(\frac{a}{R_p} \right)^2 \frac{\sqrt{1-e^2}}{\sin i} K_*, \quad (2)$$

where K_* is the stellar velocity amplitude equal to $9.2 \pm 0.8 \text{ m s}^{-1}$ ([Bonfils et al. 2012](#)) and assuming $e = 0$ (justified by current data; see [Section 3.2](#)).

The equilibrium temperature, T_{eq} , was derived using the relation ([Southworth 2010](#)):

$$T_{eq} = T_{eff} \left(\frac{1-A}{4F} \right)^{1/4} \left(\frac{R_*}{2a} \right)^{1/2}, \quad (3)$$

where T_{eff} is the effective temperature of the host star at $3652 \pm 50 \text{ K}$ (See [Table 4](#)), A is the Bond albedo, and F is the heat redistribution factor. Assuming $A = 0 - 0.4$ and $F = 0.25 - 0.50$ we find the range $T_{eq} = 506\text{-}702 \text{ K}$.

We calculated the planetary mass, M_p , using the following equation ([Winn 2010](#); [Seager 2011](#)):

$$M_p = (11.18) \left(\frac{K_*}{\sin i} \right) \left(\frac{P}{1yr} \right)^{1/3} \left(\frac{M_*}{M_\odot} \right)^{2/3} M_\oplus, \quad (4)$$

where K_* is the radial velocity semi-amplitude equal to $9.2 \pm 0.8 \text{ m s}^{-1}$ ([Bonfils et al. 2012](#)). For M_* , and P , we use the values derived from our analysis (see [Table 4](#)). The resultant planetary mass is $M_p = 13.73 \pm 1.61 M_\oplus$.

Results of the M_p , R_p , $\log_{10}(g_p)$ and the planetary density (ρ_p) from our analysis are summarized in [Table 3](#). We find a planetary radius of $R_p = 3.88 \pm 0.32 R_\oplus$.

4.3. Atmospheric Constraints

The result of this work compared with previous optical and near-IR studies ([Bonfils et al. 2012](#); [Fukui et al. 2013](#); [Crossfield et al. 2013](#)) indicates GJ 3470b appears to have a planetary radius independent of wavelength in the optical through near-IR wavelengths accessible from the ground. However, the recent publication by [Nascimbeni et al. \(2013\)](#) indicates GJ 3470b’s radius increases in the direction of the blue side of the spectrum, exhibiting a color dependence. The recent estimate on the low mean molecular weight of GJ 3470b ([Nascimbeni et al. 2013](#)) favors an atmosphere dominated by clouds or haze. It is interesting to note that the atmospheric models presented by [Nascimbeni et al. \(2013\)](#) do not predict the K-band measurements of [Crossfield et al. \(2013\)](#), just as [Crossfield et al. \(2013\)](#)’s models do not predict the U-band measurement of [Nascimbeni et al. \(2013\)](#).

We compare the full ensemble of transit observations of GJ 3470b to a set of model atmospheric transmission spectra. For this purpose, we used the atmospheric models of GJ 3470b presented

in [Crossfield et al. \(2013\)](#), which provide model observed transmission spectra after computing self-consistent equilibrium atmospheric chemistry and thermal structure. We allow each model to be scaled by a constant multiplicative factor to account for differences of a few percent between the observed and modeled transit depths. In light of the recent detection of Rayleigh scattering ([Nascimbeni et al. 2013](#)) we include a second analysis in which an ad-hoc Rayleigh-scattering haze is added to each transmission spectrum by allowing the slope and offset of the Rayleigh-scattering signature to vary in each fit. We parametrize the haze signature as $R_p^{haze} = A - B \ln \frac{\lambda}{1 \mu\text{m}}$ ([Lecavelier Des Etangs et al. 2008](#)), and take as our final transmission model the greater value of R_p^{haze} or the original model at each wavelength. Thus our haze model is not physically self-consistent, but it captures the essential features observed. For each hazy or haze-free model we computed χ^2 and the Bayesian Information Criterion ($\text{BIC} = \chi^2 + k \ln n$ when fitting n measurements with a k -dimensional model; [Schwarz 1978](#)), which penalizes models that use too many parameters. Thus, $k = 3$ for the hazy models and unity for the haze-free models.

The results of this analysis are compiled in [Table 5](#) and we show the three best-fitting models in [Figure 6](#). The best models all include a Rayleigh-scattering haze, consistent with the results of [Nascimbeni et al. \(2013\)](#). Although the hazy models with supersolar metallicities give a lower χ^2 and BIC than the hazy solar-abundance model, the difference is too small to conclusively determine whether GJ 3470b has a metal-rich atmosphere as do Uranus and Neptune ([Lunine 1993](#)) and as proposed for hot Neptune GJ 436b ([Moses et al. 2013](#); [Fortney et al. 2013](#)).

5. Conclusion

The collection of transits in this work, with the inclusion of the discovery and previously published data, provides improved parameters for the GJ 3470 system and a consistency in the analysis process. In this study we derived a new set of planetary parameters $M_p = 13.73 \pm 1.61 M_\oplus$, $R_p = 3.88 \pm 0.32 R_\oplus$, and $\rho_p = 1.18 \pm 0.33 \text{ g cm}^{-3}$, all of which are listed in [Table 3](#). We also present, to date, the most precise new transit ephemeris for this system and find an updated period of $3.3366487^{+0.0000043}_{-0.0000033}$ d. Our analysis of possible transit timing variations indicates little deviation from our calculated ephemeris, but future observations are encouraged to confirm whether or not there are other planetary bodies orbiting GJ 3470.

One benefit of a spectroscopic analysis is the opportunity to provide improved constraints on the host star’s properties. The planetary parameters are known only to the accuracy with which we know the star, so it is extremely important to know these values as well. The distance determined agrees with the value found in [Pineda et al. \(2013\)](#). The stellar mass, radius, density, and metallicity (see [Table 3](#)) have been updated using a weighted average of our derived stellar parameters and those found in [Demory et al. \(2012\)](#) and [Fukui et al. \(2013\)](#). Different methods of stellar analysis yield varying parameters appropriate for an M dwarf like GJ 3470, which motivates the need for further investigation of M dwarf stars.

This small planet lies in an observationally favorable system that presents the possibility of measuring a transmission spectrum also considered in detail by [Fukui et al. \(2013\)](#), [Crossfield et al. \(2013\)](#), and [Nascimbeni et al. \(2013\)](#)². Our second analysis of the entire collection of transit observation agrees with the results of [Nascimbeni et al. \(2013\)](#), suggesting a H₂ dominated Rayleigh-scattering haze. Further observations with higher precision and/or at shorter wavelengths will be necessary to confirm the steep Rayleigh scattering slope supported in this work and also by [Nascimbeni et al. \(2013\)](#), and to search for molecular absorption features in the planet’s transmission spectrum.

Acknowledgements

We sincerely thank all of the respective TAC committees responsible for allocating time on the facilities used in our study, as well as the telescope day crews. Special thanks to Dr. Elizabeth Green for exchanging observing nights at the Kuiper 1.6 m Telescope to acquire a transit and Rob Zellem for insightful discussion. These results made use of Lowell Observatory’s Discovery Channel Telescope, supported by Lowell, Discovery Communications, Boston University, the University of Maryland, and the University of Toledo. The Large Monolithic Imager (LMI) was funded by the National Science Foundation through grant AST-1005313. We also gratefully acknowledge the support from the University of Arizona Astronomy Club. The following internet-based resources were used in this paper: the SIMBAD database operated by CDS, the ArXiv scientific paper preprint service operated by Cornell University and the ADS operated by the Harvard-Smithsonian Center for Astrophysics.

REFERENCES

- Agol, E., Steffen, J., Sari, R., & Clarkson, W. 2005, *MNRAS*, 359, 567
- Aldering, G., Adam, G., Antilogus, P., et al. 2002, in *Proc. SPIE*, ed. J. A. Tyson & S. Wolff, Vol. 4836, 61–72
- Aldering, G., Antilogus, P., Bailey, S., et al. 2006, *ApJ*, 650, 510
- Allard, F., Homeier, D., & Freytag, B. 2011, in *Astronomical Society of the Pacific Conference Series*, Vol. 448, 16th Cambridge Workshop on Cool Stars, Stellar Systems, and the Sun, ed. C. Johns-Krull, M. K. Browning, & A. A. West, 91
- Allard, F., Homeier, D., Freytag, B., et al. 2013, *Memorie della Societa Astronomica Italiana Supplementi*, 24, 128
- Bacon, R., Copin, Y., Monnet, G., et al. 2001, *MNRAS*, 326, 23
- Batalha, N. M., Rowe, J. F., Bryson, S. T., et al. 2013, *ApJS*, 204, 24
- Berta, Z. K., Charbonneau, D., Bean, J., et al. 2011, *ApJ*, 736, 12
- Bessell, M. S. 1999, *PASP*, 111, 1426
- Bochanski, J. J., West, A. A., Hawley, S. L., & Covey, K. R. 2007, *AJ*, 133, 531
- Bonfils, X., Gillon, M., Udry, S., et al. 2012, *A&A*, 546, A27
- Boyajian, T. S., von Braun, K., van Belle, G., et al. 2012, *ApJ*, 757, 112
- Brown, T. M., Baliber, N., Bianco, F. B., et al. 2013, *ArXiv e-prints*, arXiv:1305.2437

²Our conclusions are consistent with those of [Ehrenreich et al. \(2014\)](#), which we became aware of seven months after the submission of our work.

- Butler, R. P., Vogt, S. S., Marcy, G. W., et al. 2004, *ApJ*, 617, 580
- Buton, C., Copin, Y., Aldering, G., et al. 2013, *A&A*, 549, A8
- Carter, J. A., & Winn, J. N. 2009, *ApJ*, 704, 51
- Castelli, F., & Kurucz, R. L. 2004, *ArXiv Astrophysics e-prints*, arXiv:astro-ph/0405087
- Charbonneau, D., Berta, Z. K., Irwin, J., et al. 2009, *Nature*, 462, 891
- Ciceri, S., Mancini, L., Southworth, J., et al. 2013, *A&A*, 557, A30
- Crossfield, I. J. M. 2012, *A&A*, 545, A97
- Crossfield, I. J. M., Barman, T., Hansen, B. M. S., & Howard, A. W. 2013, *ArXiv e-prints*, arXiv:1308.6580
- Cushing, M. C., Vacca, W. D., & Rayner, J. T. 2004, *PASP*, 116, 362
- Czesla, S., Huber, K. F., Wolter, U., Schröter, S., & Schmitt, J. H. M. M. 2009, *A&A*, 505, 1277
- Dawson, R. I., & Fabrycky, D. C. 2010, *ApJ*, 722, 937
- Delorme, P., Collier Cameron, A., Hebb, L., et al. 2011, *MNRAS*, 413, 2218
- Deming, D., Richardson, L. J., & Harrington, J. 2007, *MNRAS*, 378, 148
- Demory, B.-O., Gillon, M., Barman, T., et al. 2007, *A&A*, 475, 1125
- Demory, B.-O., Gillon, M., Deming, D., et al. 2011, *A&A*, 533, A114
- Demory, B.-O., Gillon, M., Bonfils, X., et al. 2012, *Spitzer Proposal*, 80261
- Demory, B.-O., Torres, G., Neves, V., et al. 2013, *ApJ*, 768, 154
- Dong, S., & Zhu, Z. 2012, *ArXiv e-prints*, arXiv:1212.4853
- Dragomir, D., Matthews, J. M., Winn, J. N., Rowe, J. F., & MOST Science Team. 2013, *ArXiv e-prints*, arXiv:1302.3321
- Dressing, C. D., & Charbonneau, D. 2013, *ApJ*, 767, 95
- Eaton, J. A., Henry, G. W., & Fekel, F. C. 2003, in *Astrophysics and Space Science Library*, Vol. 288, *Astrophysics and Space Science Library*, ed. T. D. Oswalt
- Ehrenreich, D., Bonfils, X., Lovis, C., et al. 2014, *ArXiv e-prints*, arXiv:1405.1056
- Flower, P. J. 1996, *ApJ*, 469, 355
- Fortney, J. J., Mordasini, C., Nettelmann, N., et al. 2013, *ApJ*, 775, 80
- Fukui, A., Narita, N., Kurosaki, K., et al. 2013, *ApJ*, 770, 95
- Gazak, J. Z., Johnson, J. A., Tonry, J., et al. 2012, *Advances in Astronomy*, 2012, arXiv:1102.1036
- Gillon, M., Pont, F., Demory, B.-O., et al. 2007, *A&A*, 472, L13
- Guillot, T., & Havel, M. 2011, *A&A*, 527, A20
- Hamuy, M., Walker, A. R., Suntzeff, N. B., et al. 1992, *PASP*, 104, 533
- Henry, G. W. 1999, *PASP*, 111, 845
- Henry, G. W., Fekel, F. C., & Hall, D. S. 1995, *AJ*, 110, 2926
- Holman, M. J., & Murray, N. W. 2005, *Science*, 307, 1288
- Howard, A. W., Johnson, J. A., Marcy, G. W., et al. 2011, *ApJ*, 730, 10
- Howard, A. W., Marcy, G. W., Bryson, S. T., et al. 2012, *ApJS*, 201, 15
- Irwin, J., Berta, Z. K., Burke, C. J., et al. 2011, *ApJ*, 727, 56
- Johnson, J. A., Apps, K., Gazak, J. Z., et al. 2011, *ApJ*, 730, 79
- Jordán, A., Espinoza, N., Rabus, M., et al. 2013, *ApJ*, 778, 184

- Knutson, H. A., Madhusudhan, N., Cowan, N. B., et al. 2011, *ApJ*, 735, 27
- Lantz, B., Aldering, G., Antilogus, P., et al. 2004, in *Society of Photo-Optical Instrumentation Engineers (SPIE) Conference Series*, Vol. 5249, *Society of Photo-Optical Instrumentation Engineers (SPIE) Conference Series*, ed. L. Mazuray, P. J. Rogers, & R. Wartmann, 146–155
- Lecavelier Des Etangs, A., Pont, F., Vidal-Madjar, A., & Sing, D. 2008, *A&A*, 481, L83
- Lépine, S., Hilton, E. J., Mann, A. W., et al. 2013, *AJ*, 145, 102
- Lunine, J. I. 1993, *ARA&A*, 31, 217
- Mancini, L., Southworth, J., Ciceri, S., et al. 2013, *A&A*, 551, A11
- Mandel, K., & Agol, E. 2002, *ApJ*, 580, L171
- Mann, A. W., Brewer, J. M., Gaidos, E., Lépine, S., & Hilton, E. J. 2013a, *AJ*, 145, 52
- Mann, A. W., Gaidos, E., & Ansdell, M. 2013b, *ApJ*, 779, 188
- Mann, A. W., Gaidos, E., Lépine, S., & Hilton, E. J. 2012, *ApJ*, 753, 90
- McArthur, B. E., Endl, M., Cochran, W. D., et al. 2004, *ApJ*, 614, L81
- McQuillan, A., Aigrain, S., & Mazeh, T. 2013, *MNRAS*, 432, 1203
- Meibom, S., Mathieu, R. D., & Stassun, K. G. 2009, *ApJ*, 695, 679
- Meschiari, S., Wolf, A. S., Rivera, E., et al. 2009, *PASP*, 121, 1016
- Moses, J. I., Line, M. R., Visscher, C., et al. 2013, *ApJ*, 777, 34
- Nascimbeni, V., Piotto, G., Pagano, I., et al. 2013, *ArXiv e-prints*, arXiv:1308.6765
- Oke, J. B. 1990, *AJ*, 99, 1621
- Paulson, D. B., Saar, S. H., Cochran, W. D., & Henry, G. W. 2004, *AJ*, 127, 1644
- Pearson, K. A., Turner, J. D., & Sagan, T. A. G. 2013, *ArXiv e-prints*, arXiv:1310.5397
- Pineda, J. S., Bottom, M., & Johnson, J. A. 2013, *ApJ*, 767, 28
- Pont, F., Sing, D. K., Gibson, N. P., et al. 2013, *MNRAS*, 432, 2917
- Pont, F., Gilliland, R. L., Moutou, C., et al. 2007, *A&A*, 476, 1347
- Queloz, D., Henry, G. W., Sivan, J. P., et al. 2001, *A&A*, 379, 279
- Rabus, M., Alonso, R., Belmonte, J. A., et al. 2009, *A&A*, 494, 391
- Rayner, J. T., Cushing, M. C., & Vacca, W. D. 2009, *ApJS*, 185, 289
- Rayner, J. T., Toomey, D. W., Onaka, P. M., et al. 1998, in *Society of Photo-Optical Instrumentation Engineers (SPIE) Conference Series*, Vol. 3354, *Society of Photo-Optical Instrumentation Engineers (SPIE) Conference Series*, ed. A. M. Fowler, 468–479
- Schwarz, G. 1978, *The Annals of Statistics*, 6, 461
- Seager, S. 2011, *Exoplanets*, ed. Piper, S.
- Seager, S., & Mallén-Ornelas, G. 2003, *ApJ*, 585, 1038
- Southworth, J. 2010, *MNRAS*, 408, 1689
- Southworth, J., Wheatley, P. J., & Sams, G. 2007, *MNRAS*, 379, L11
- Southworth, J., Hinse, T. C., Jørgensen, U. G., et al. 2009, *MNRAS*, 396, 1023
- Stetson, P. B. 1987, *PASP*, 99, 191
- Stoughton, C., Lupton, R. H., Bernardi, M., et al. 2002, *AJ*, 123, 485
- Vaniček, P. 1971, *Ap&SS*, 12, 10

Winn, J. N. 2010, ArXiv e-prints, arXiv:1001.2010

Winn, J. N., Matthews, J. M., Dawson, R. I., et al. 2011, ApJ, 737, L18

Wright, E. L., Eisenhardt, P. R. M., Mainzer, A. K., et al. 2010, AJ, 140, 1868

Table 1. Individual Transit Log and Parameters

Transit	Date (UT)	Filter	Telescope	Exposure Time	Airmass	Seeing	R_p/R_\star	T_{mid} [BJD _{TDB} – 2450000]
01 ^a	2012 Feb 26	Gunn Z	Trappist	10s	1.4-1.9	-	$0.0766^{+0.0019}_{-0.0020}$	5983.7417 ± 0.0015
02 ^a	2012 Mar 07	Gunn Z	EulerCam	50s	>3.55	-	$0.0766^{+0.0019}_{-0.0020}$	5993.7141 ± 0.0015
03 ^a	2012 Mar 07	Gunn Z	Trappist	10s	>3.04	-	$0.0766^{+0.0019}_{-0.0020}$	5993.7141 ± 0.0015
04 ^b	2012 Nov 15	I _c	MITSuME	60s	1.06-1.28	defocused	$0.0780^{+0.0015}_{-0.0016}$	$6247.29954^{+0.00028}_{-0.00029}$
05 ^b	2012 Nov 15	J	ISLE	30s	1.06-1.42	defocused	$0.0757^{+0.0012}_{-0.0013}$	$6247.29954^{+0.00028}_{-0.00029}$
06 ^b	2012 Nov 15	R _c	MITSuME	60s	1.06-1.28	defocused	$0.0752^{+0.0039}_{-0.0044}$	$6247.29954^{+0.00028}_{-0.00029}$
07 ^b	2012 Nov 15	g'	MITSuME	60s	1.06-1.28	dofocused	$0.0786^{+0.0080}_{-0.011}$	$6247.29954^{+0.00028}_{-0.00029}$
08	2012 Nov 22	Gunn Z	Nickel	65s	1.0-1.2	1.5"	$0.0766^{+0.0019}_{-0.0020}$	$6253.9729^{+0.0011}_{-0.0013}$
09	2013 Jan 08	r'	LSC	20s	1.0-1.8	2.7"	0.0803 ± 0.0025	$6300.68551^{+0.00063}_{-0.00068}$
10	2013 Jan 08	Panstarrs-Z	LSC	30s	1.0-1.8	2.2"	$0.0766^{+0.0019}_{-0.0020}$	$6300.68551^{+0.00063}_{-0.00068}$
11	2013 Jan 18	I	DCT	10s	1.1-2.0	defocused	$0.0780^{+0.0015}_{0.0016}$	$6310.69616^{+0.00032}_{-0.00031}$
12	2013 Jan 18	Gunn Z	Nickel	65s	1.3-2.0	1.5"	$0.0766^{+0.0019}_{-0.0020}$	$6310.69616^{+0.00032}_{-0.00031}$
13 ^c	2013 Feb 17	LBC Uspec	LBT	60s	1.0-1.2	defocused	0.0792 ± 0.0019	$6340.72589^{+0.00012}_{-0.00013}$
14 ^c	2013 Feb 17	LBC F972N20	LBT	60s	1.0-1.2	defocused	0.07430 ± 0.00072	$6340.72589^{+0.00012}_{-0.00013}$
15	2013 Feb 17	Arizona-I	Kuiper	07s	1.04-1.27	1.43"	$0.0736^{+0.0029}_{-0.0031}$	$6340.72589^{+0.00012}_{-0.00013}$
16	2013 Feb 27	Gunn Z	Nickel	65s	1.0-1.2	1.5"	$0.0766^{+0.0019}_{-0.0020}$	$6350.73524^{+0.00088}_{-0.00090}$
17	2013 Mar 09	Bessel-B	FTN	180s	1.0-1.1	2.7"	$0.084^{+0.013}_{-0.016}$	$6360.7449^{+0.0012}_{-0.0015}$
18	2013 Mar 09	r'	ELP	30s	1.0-1.7	defocused	0.0803 ± 0.0025	$6360.7449^{+0.0012}_{-0.0015}$
19	2013 Mar 15	Cousins I	CAHA 1.23-m	120s	1.11-1.15	defocused	$0.0780^{+0.0015}_{-0.0016}$	$6367.41949^{+0.00045}_{-0.00043}$
20	2013 Mar 19	i'	ELP	45s	1.0-2.6	defocused	$0.0765^{+0.0027}_{-0.0030}$	$6370.75641^{+0.00081}_{-0.00076}$
21	2013 Mar 29	r'	ELP	45s	1.0-2.9	defocused	0.0803 ± 0.0025	$6380.76480^{+0.00083}_{-0.00080}$

^aFirst presented by [Bonfils et al. \(2012\)](#), reanalyzed here.

^bFirst presented by [Fukui et al. \(2013\)](#), reanalyzed here.

^cFirst presented by [Nascimbeni et al. \(2013\)](#), reanalyzed here.

Table 2. Filter-Specific Quadratic Limb-Darkening Coefficients

Filter	Telescope	Best Fit ^{a,d}	PHOENIX ^{b,d}	Kurucz ^{c,d}
r'	ELP/LSC	$0.403^{+0.040}_{-0.044}$, $0.390^{+0.036}_{-0.038}$	0.386 ± 0.044 , 0.383 ± 0.032	0.391, 0.329
GunnZ	Lick, Trappist, Euler	$0.017^{+0.014}_{-0.012}$, 0.5030 ± 0.0068	0.013 ± 0.016 , 0.503 ± 0.008	0.224, 0.424
Panstarrs-Z	LSC	$0.029^{+0.025}_{-0.018}$, 0.5030 ± 0.014	0.022 ± 0.017 , 0.522 ± 0.007	0.119, 0.487
I	DCT, CAHA	0.070 ± 0.025 , $0.517^{+0.010}_{-0.0099}$	0.066 ± 0.019 , 0.517 ± 0.007	0.100, 0.484
Arizona-I	Kuiper	$0.083^{+0.035}_{-0.032}$, 0.519 ± 0.016	0.075 ± 0.019 , 0.518 ± 0.008	0.179, 0.439
i'	ELP	$0.123^{+0.038}_{-0.047}$, 0.488 ± 0.020	0.123 ± 0.021 , 0.489 ± 0.010	0.230, 0.422
J	Okayama	$0.023^{+0.018}_{-0.013}$, 0.383 ± 0.012	-0.009 ± 0.014 , 0.383 ± 0.006	-0.119, 0.510
g'	Mitsume	0.359 ± 0.063 , $0.412^{+0.051}_{-0.054}$	0.359 ± 0.034 , 0.410 ± 0.026	0.392, 0.401
Rc	Mitsume	$0.330^{+0.091}_{-0.069}$, 0.369 ± 0.059	0.371 ± 0.039 , 0.373 ± 0.030	0.409, 0.302
Ic	Mitsume	$0.084^{+0.038}_{-0.035}$, $0.5130^{+0.016}_{-0.017}$	0.082 ± 0.020 , 0.512 ± 0.008	0.203, 0.423

^aFinal LD coefficients from TAP analysis using the PHOENIX priors shown.

^bReference [Allard et al. \(2011\)](#).

^cReference [Castelli & Kurucz \(2004\)](#).

^dThe order of the coefficients listed: first = linear, second = quadratic.

Table 3. Adopted System Parameters

Parameter	Value	Units
<i>Stellar parameters</i>		
Effective Temperature ^b T_{eff}	3652 ± 50	K
Metallicity ^b [Fe/H]	0.17 ± 0.06	-
Mean density ^b ρ_{\star}	$3.39^{+0.30}_{-0.32}$	ρ_{\odot}
Stellar Surface Gravity $\log_{10}(g)$	4.78 ± 0.12	cgs
Mass M_{\star}	0.51 ± 0.06	M_{\odot}
Radius R_{\star}	0.48 ± 0.04	R_{\odot}
Distance ^a	28.82 ± 2.53	pc
Rotation Period	20.70 ± 0.15	d
Age	1-4	Gyr
<i>Planetary parameters^a</i>		
Scaled Semi-major Axis a/R_{\star}	$13.94^{+0.44}_{-0.49}$	-
Planet-Star Radius Ratio R_p/R_{\star}	0.07642 ± 0.00037	-
Mid Transit Time T_o	$2455983.70472 \pm 0.00021$	BJD _{TDB}
Orbital Period P	$3.3366487^{+0.0000043}_{-0.0000033}$	d
Orbital Inclination i	$88.88^{+0.62}_{-0.45}$	deg
Semi-major axis a	0.031 ± 0.0028	AU
Impact Parameter $b = a \cos i/R_{\star}$	0.29 ± 0.14	-
Mean density ρ_p	1.18 ± 0.33	g cm^{-3}
Surface gravity $\log_{10}(g)$	2.83 ± 0.11	cgs
Mass M_p	13.73 ± 1.61	M_{\oplus}
Radius R_p	3.88 ± 0.32	R_{\oplus}
Eccentricity e	$0.017^{+0.016}_{-0.012}$	-
Periastron ω	$1.70^{+0.96}_{-1.20}$	deg
T_{eq}	506 - 702	K

^aThe uncertainty in these values are dominated by the uncertainty in the stellar parameters in [Section 4.2](#).

^bThe value for stellar density displayed in this table is the weighted mean of the densities yielded by both the light curves and the spectra in this work. T_{eff} and [Fe/H] provided above are the weighted averages of all previous works, found in [Table 4](#).

Table 4. Stellar Parameters

Reference	Radius [R_{\odot}]	Mass [M_{\odot}]	Stellar Density [ρ_{\odot}]	Effective Temperature [K]	[Fe/H]
Bonfils et al. 2012	0.503 ± 0.063	0.541 ± 0.067	4.26 ± 0.53	3600 ± 200	-
Demory et al. 2012	0.568 ± 0.037	0.539 ± 0.047	2.91 ± 0.37	3600 ± 100	0.2 ± 0.10
Fukui et al. 2013	0.563 ± 0.024	0.594 ± 0.029	3.32 ± 0.27	-	-
Pineda et al. 2013	0.500 ± 0.050	0.530 ± 0.050	4.25 ± 0.40	-	0.12 ± 0.12
Crossfield et al. 2013	-	-	3.49 ± 1.13	-	-
Nascimbeni et al. 2013	-	-	2.74 ± 0.19	-	-
This Work (spectroscopic analysis)	0.48 ± 0.04	0.51 ± 0.06	4.62 ± 1.10	3682 ± 60	0.18 ± 0.08
This Work (light curves)	-	-	$3.27^{+0.31}_{-0.34}$	-	-

Table 5. Atmospheric Model Fits

Model Name	χ^2	BIC
Hazy, 50× solar	8.80	17.30
Hazy, 200× solar	15.27	23.77
Hazy, Solar	19.15	27.65
200× solar	29.31	32.14
Flat	32.73	35.56
Hazy, Solar, no CH ₄	27.49	35.99
Hazy, Solar, no C	28.66	37.16
Solar, no CH ₄	38.83	41.66
Solar, no C	39.59	42.43
Hazy, 200×, no C	33.94	42.44
50× solar	39.90	42.73
Hazy, 50×, no C	39.97	48.47
200×, no C	45.83	48.67
50×, no C	57.02	59.86
Solar	62.79	65.62

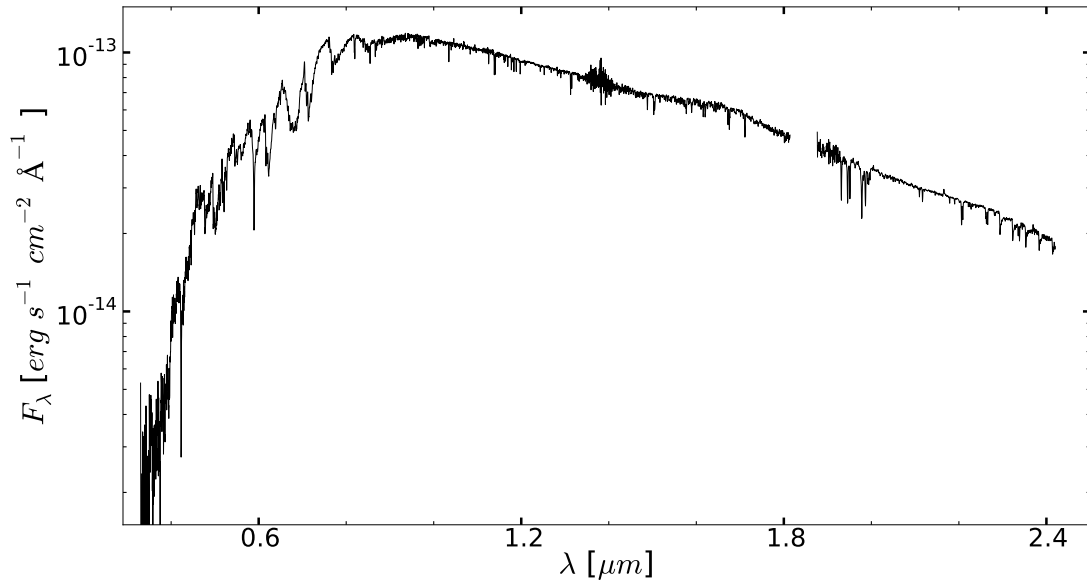


Fig. 1.— The stellar spectrum of GJ 3470 from 0.33 to 2.42 μm obtained with UH 2.2m/SNIFS (0.33 – 0.9 μm) and IRTF/SpeX (0.9 – 2.4 μm). The noisy regions around 1.4 μm and 1.9 μm are due to telluric contamination. These data are available as an electronic supplement to the paper.

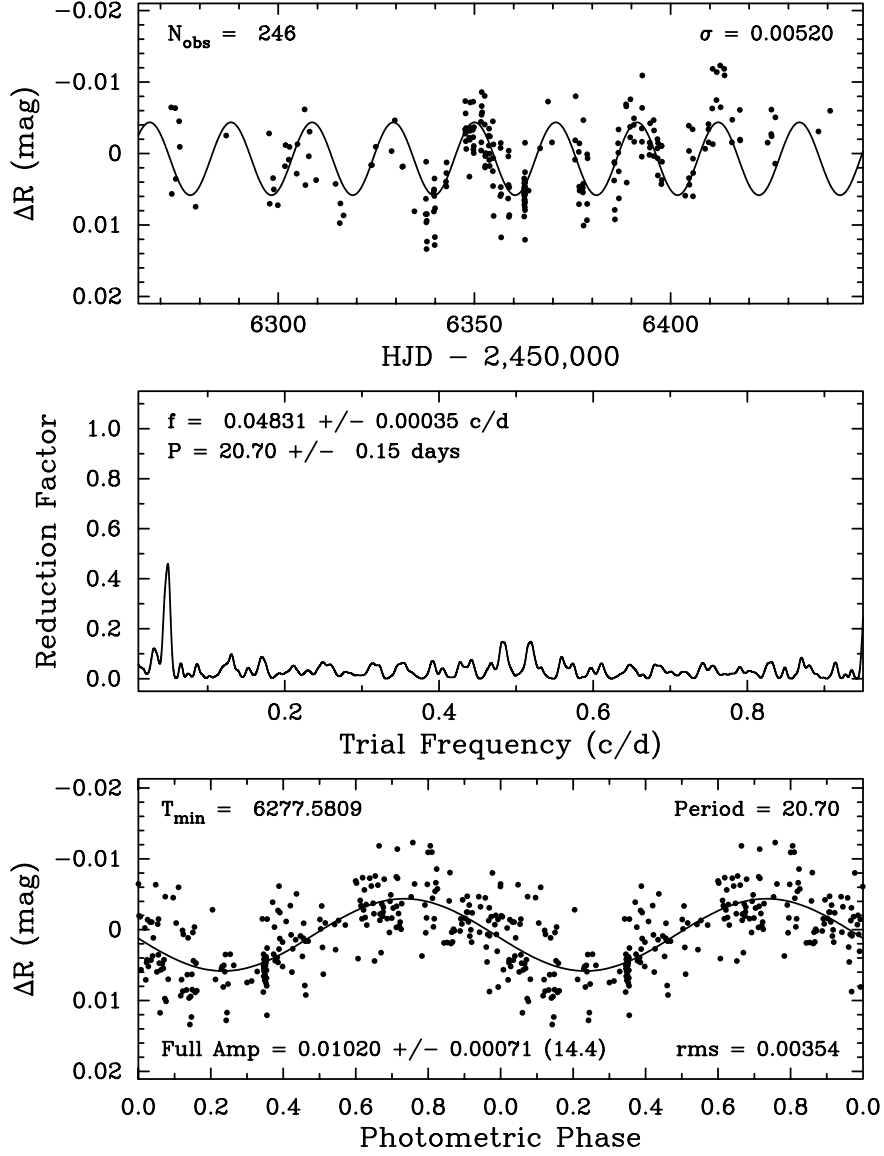


Fig. 2.— *Top*: The Cousins R band photometry of GJ 3470 (see Section 2.2) from 2012–2013 acquired with the C14 0.36 m automated imaging telescope at Fairborn Observatory. Slow brightness variability of 0.01 mag or so is apparent. *Middle*: Frequency spectrum of the C14 observations gives a stellar rotation period of 20.70 ± 0.15 d. *Bottom*: A least-squares sine fit of the C14 observations phased with 20.70-day rotation period shows reasonable coherence over the 2012–2013 observing season. This same sine curve is laid over the photometric observations in the top panel and also shows good coherence in spite of the small spot amplitude.

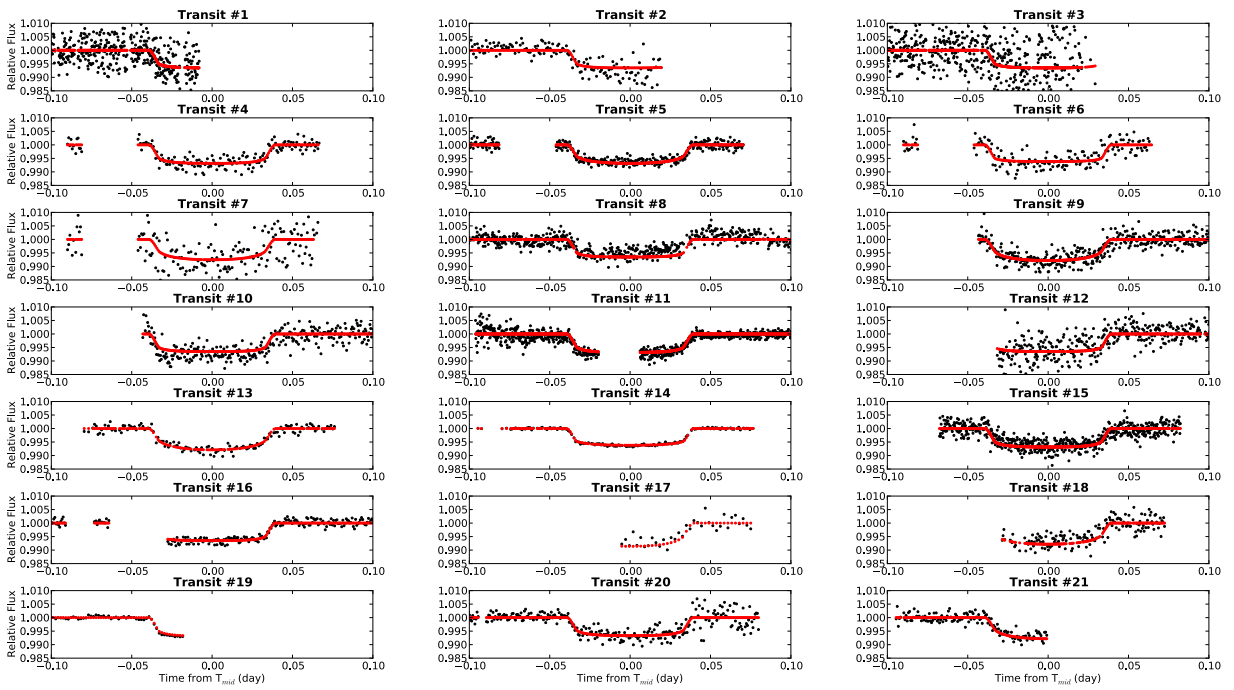


Fig. 3.— Individual light curves of GJ 3470b are associated with the transit number found in Table 1. The best-fit model is shown as a solid red line. These data and the residuals are available as an electronic supplement to the paper.

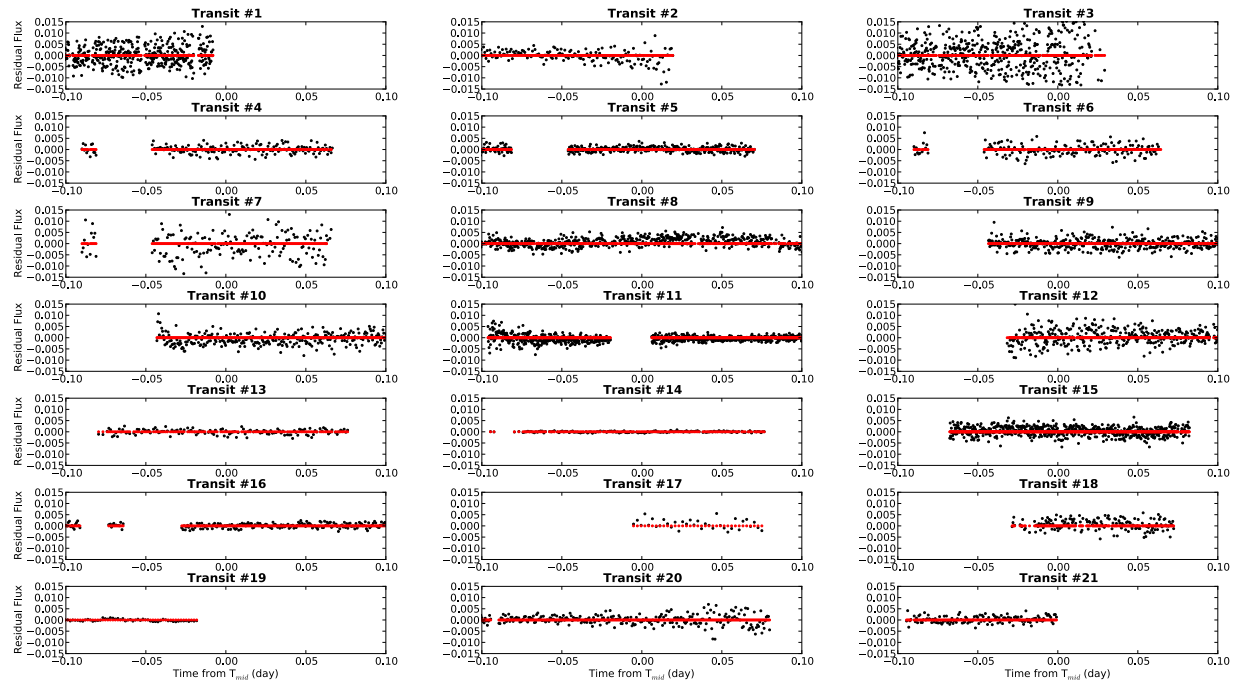


Fig. 4.— Corresponding residuals for the individual light curves in Figure 3.

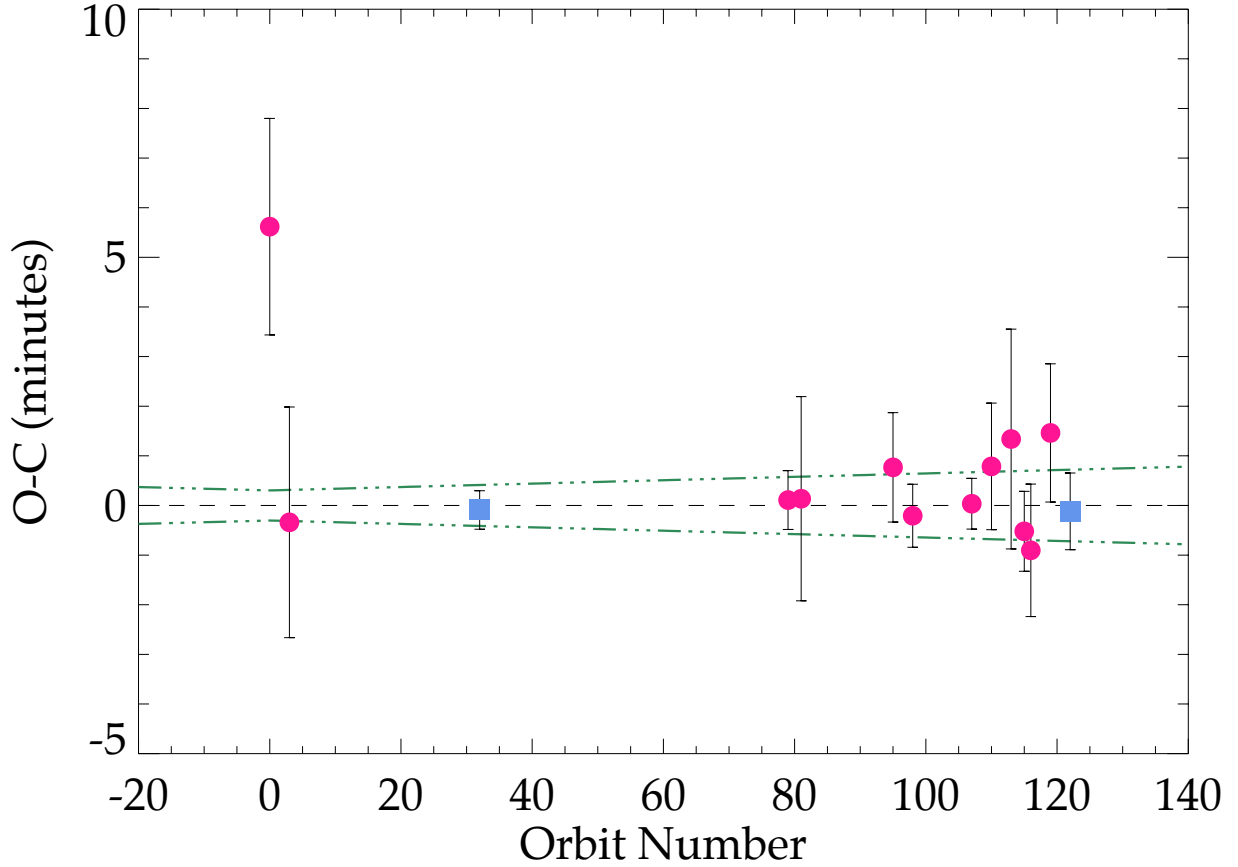


Fig. 5.— A plot of the observed minus the calculated mid-transit times, where the magenta circles indicate data modeled in this work with TAP, while the blue squares were modeled separately by Demory et al. (2013) and Crossfield et al. (2013). Multiple transits taken at a given epoch share a similar datapoint. The region outlined in green gives the range of non-TTVs (within 1σ of the error of the period) for each orbit number, beginning with the discovery transit. Values lying outside of this region indicate the occurrence of a TTV. Transit 1 exhibits a low quality, partial light curve; even though it lies outside the region in green, we disregard this point as a TTV.

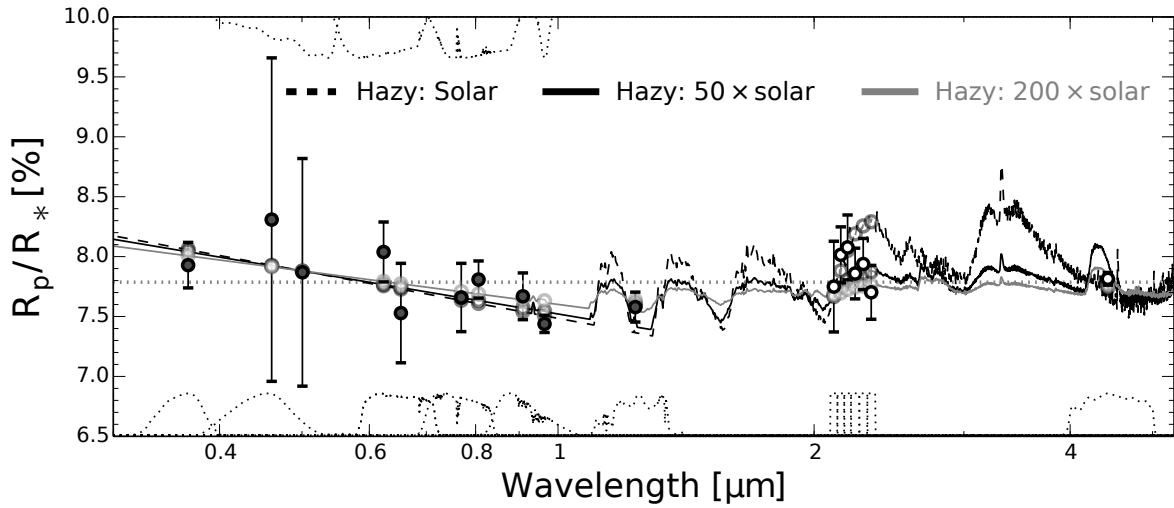


Fig. 6.— Transmission spectrum of GJ 3470b. Solid points with error bars are our measurements; open points with error bars are previous infrared measurements (Demory et al. 2013; Crossfield et al. 2013). The solid lines show the three best-fit model transmission spectra described in Section 4.3 and Table 5. These models all include a Rayleigh-scattering slope at shorter wavelengths; no molecular features are yet detected at longer wavelengths. The dotted lines at bottom and top show all filter profiles used in this analysis; we use these to compute the band-integrated model points (shown as colored open circles).